

An intelligent device with double fluorescent carbon dots based on smartphone for visual and point-of-care testing of Copper(II) in water and food samples

Tiange Li^a, Tiantian Wu^a, Meiju Lu^a, Ning Li^a, Yan Ma^a, Lianjun Song^a, Xianqing Huang^a, Jiansheng Zhao^b, Tianlin Wang^{a,*}

^a Henan Engineering Technology Research Center of Food Processing and Circulation Safety Control, College of Food Science and Technology, Henan Agricultural University, Zhengzhou 450002, China

^b Henan Shuanghui Investment & Development Co., Ltd., Luohe 462000, China

ARTICLE INFO

Keywords:

Carbon dots
Ratiometric fluorescence
Intelligent device
Point-of-care testing
Copper (II)

ABSTRACT

The excessive presence of Cu^{2+} could be harmful to human health. Therefore, a ratiometric fluorescence sensor based on multicolor fluorescent carbon dots (CDs) was developed for Cu^{2+} detection. The blue and yellow carbon dots (B-CDs/Y-CDs) were synthesized by one-step hydrothermal method. After adding Cu^{2+} , it is captured by the amino groups of B-CDs to form complexes, resulting in a strong fluorescence quenching via photoinduced electron transfer (PET). Meanwhile, the amino groups from Y-CDs also binds with Cu^{2+} that inhibit the internal PET thus enhancing the fluorescence of Y-CDs. The sensor has the merits in rapid, visual, and selective with a low limit of detection (LOD) at 2.29 nM. Furthermore, an intelligent device composed of portable optical detector and smartphone is constructed, which realizes the visual point-of-care testing (POCT) of Cu^{2+} with a LOD of 7.51 nM. The strategy provides an accessible approach for monitoring heavy metal pollution and food safety.

1. Introduction

Copper ion as one of indispensable nutrient with human and animals and plants life activities, can regulate various physiological functions of the human bodies (Chen et al., 2023; Zuo et al., 2023). However, insufficient or excess of Cu^{2+} can lead to many diseases, such as Wilson's disease, Menkes disease, cardiovascular disease, and cancer (Lu, Wei, et al., 2023; Lu, Zhang, et al., 2023; Zhao et al., 2021). In addition, copper ions could easily accumulate in water, fruits, vegetables and aquatic animals through the food chain, eventually endangering human health (Liu, Hao, et al., 2023). Therefore, rapid and sensitive detection of Cu^{2+} ions is very important for environmental protection and human health.

Since a long time ago, some classic methods have been developed for Cu^{2+} detection, such as inductively coupled plasma mass spectrometry (ICP-MS) (Lu, Wei, et al., 2023), atomic absorption spectrometry (AAS) (Pourbasheer et al., 2022), inductively coupled plasma atomic emission spectrometry (ICP-AES) (Lledó et al., 2023), electrochemical (Moussaoui et al., 2023), etc. Although these methods can achieve precise quantitative detection of Cu^{2+} , the drawbacks in large and

expensive instrument, time-consuming operation and maintenance problems hindered their application in point-of-care testing (POCT) of Cu^{2+} . POCT requires the development of detection methods that are fast, convenient, and accurate (Zeng et al., 2024). Satisfyingly, the development of fluorescence sensors based on fluorescent nanomaterials could meet all the requirements of POCT (Wang et al., 2024). In particular, the fluorescence color changes caused by fluorescent sensors in detecting Cu^{2+} is observed by naked-eye, making them occupy an important position in visual POCT (Xu et al., 2023).

Carbos dots (CDs), as a classic class of fluorescent nanomaterials (Alafeef et al., 2024), have the characteristics of good water solubility, low toxicity, easy to synthesize, and fluorescence adjustability (Liu, Guo, et al., 2023; Liu, Hao, et al., 2023; Speranskaya et al., 2020). Hence, various fluorescent sensors composed of CDs has been developed for visual analysis of Cu^{2+} . Zhang et al. prepared a N and S-doped carbon dots (N/SCDs) using *p*-phenylenediamine and 2-mercaptothiazoline for the detection of Cu^{2+} (Zhang, Xiao, et al., 2024; Zhang, Yin, et al., 2024). In addition, Ge et al. prepared N-CDs by heat treatment with hexamethylenetetramine and ammonium citrate as precursors, which has been successfully used for detection of Cu^{2+} (Ge et al., 2021). However,

* Corresponding author.

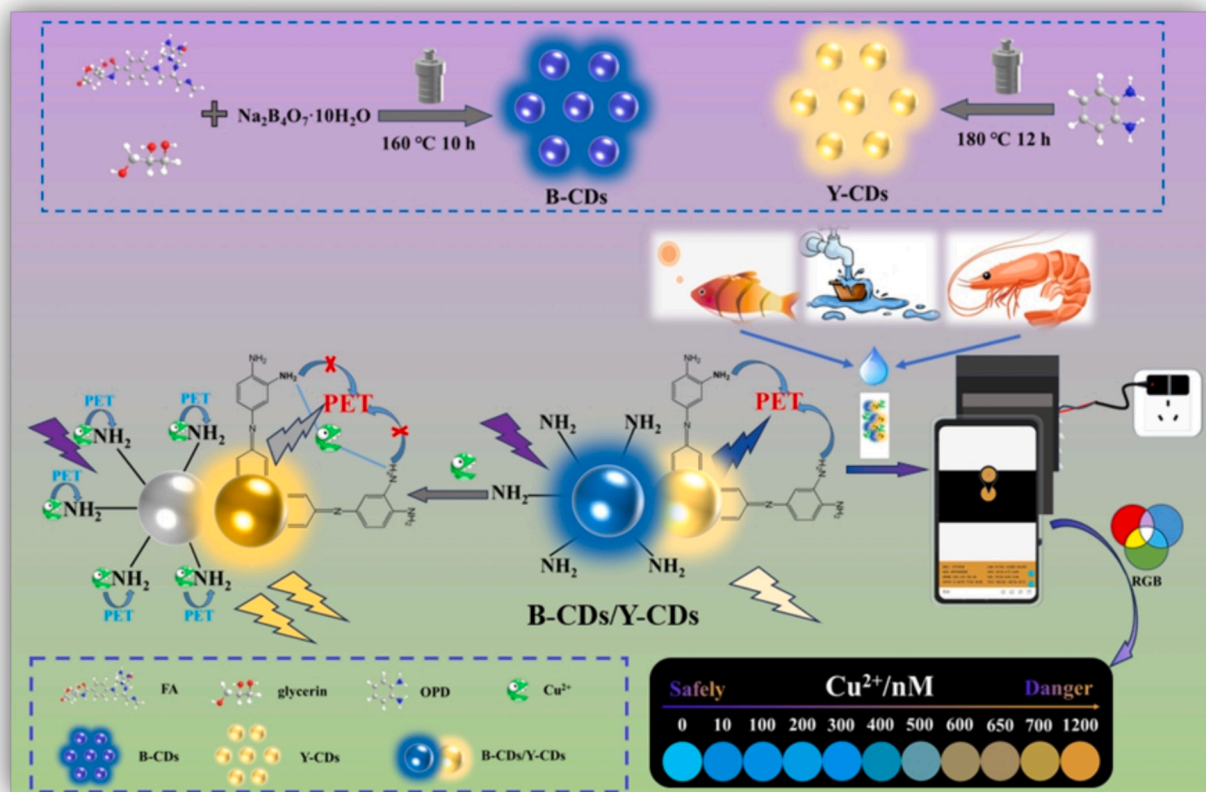
E-mail address: wang0814105@126.com (T. Wang).

<https://doi.org/10.1016/j.fochx.2024.101834>

Received 12 July 2024; Received in revised form 8 September 2024; Accepted 10 September 2024

Available online 16 September 2024

2590-1575/© 2024 The Authors. Published by Elsevier Ltd. This is an open access article under the CC BY-NC license (<http://creativecommons.org/licenses/by-nc/4.0/>).



Scheme 1. The process of detecting Cu^{2+} using B-CDs/Y-CDs sensor and intelligent device

most fluorescent sensors based CDs with single fluorescence response was easily vulnerable to accidental factors such as background signal and instrument parameters, which may result in incorrect fluorescence signal response and thereby diminishing the sensitivity and precision of the sensors (Zhang, Xiao, et al., 2024). Ratiometric fluorescence sensors with a self-calibration feature are developed for targets detection by monitoring changes in two fluorescent signals. They can reduce the impact of background signals and accidental factors, thus providing more accurate and reliable results (Miao et al., 2024). Actually, it is easy to obtain CDs with different fluorescence by changing the synthesized precursor based on the tunable fluorescence characteristics of CDs. Therefore, the construction of ratiometric fluorescence sensors has made it possible through the hybridizing of multiple CDs, which has become one of the most effective methods.

With the development of society towards intelligence, artificial intelligence (AI) serves various industries in society (Al Mashhadany et al., 2024). Smartphones, as a classic representative of AI products, play a crucial role in daily life and work due to its functions in communication, photography, analysis, etc. The fluorescence color can be captured and converted into red-green-blue (RGB) values by smartphones for visual quantitative and POCT of targets (Liang et al., 2024). Hence, smartphones exhibit huge potential for practical applications in detection field.

In this study, we presented a ratiometric fluorescence sensor that is based on the mixing of CDs with blue and yellow fluorescence (B-CDs and Y-CDs) for the purpose of detecting Cu^{2+} (Scheme 1). Firstly, the B-CDs and Y-CDs were synthesized through a one-step hydrothermal synthesis method. The two types of CDs mixed with each other through electrostatic adsorption, forming B-CDs/Y-CDs sensing system. It initially emits blue fluorescence of B-CDs due to the PET effect occurring within Y-CDs. Once exposed to Cu^{2+} , it will interact with the amino group on the surface of B-CDs, resulting in a PET reaction between Cu^{2+}

and B-CDs, which quenched the blue fluorescence. Meanwhile, Cu^{2+} also is captured by the amino groups of Y-CDs that suppress the PET thus enhancing the yellow fluorescence. Hence, the sensing system is quickly observed by naked eyes from blue to yellow, and shows a linear relationship with Cu^{2+} concentration within a specific range. Moreover, an intelligent device composed of optical detector and smartphone is developed for visual POCT of Cu^{2+} on site in water and foods. The strategy may provide a new tool for food safety and heavy metal pollution monitoring industry.

2. Experimental section

2.1. Chemicals

Folic acid (FA) and *o*-phenylenediamine (OPD) are purchased from MACKLIN Reagent Co., LTD. (Shanghai, China). Borax, glycerin, CuCl_2 , KCl , NaCl , PbCl_2 , CaCl_2 , MgCl_2 , CdCl_2 , BaCl_2 , ZnCl_2 , MnCl_2 , FeSO_4 and FeCl_3 are purchased from Tianjin Guangfu Fine Chemical Co., LTD., China. All reagents belong to analytical grade. All water used in the experiments is $18.2 \text{ M}\Omega \text{ cm}^{-1}$ ultra-pure water.

2.2. Instruments and measurements

The fluorescence spectra were obtained by Lumina fluorescence spectrophotometer (Thermo, Ltd., USA). The morphology of CDs was measured by JEM-2100 Pro transmission electron microscope (JEOL, Ltd., Japan). Crystal structures of CDs were determined using the Ultima IV X-ray diffractometer (kabuskiki kaisha, Ltd., Japan). The Element composition of CDs was measured by EscaLab Xi⁺ X-ray photoelectron spectroscopy (Thermo, Ltd., USA). FT-IR spectra of CDs were measured on a TENSOR 27 Fourier Transform infrared (FT-IR) spectrometer (Bruker, Ltd., Germany). In addition, the fluorescence lifetime of B-CDs,

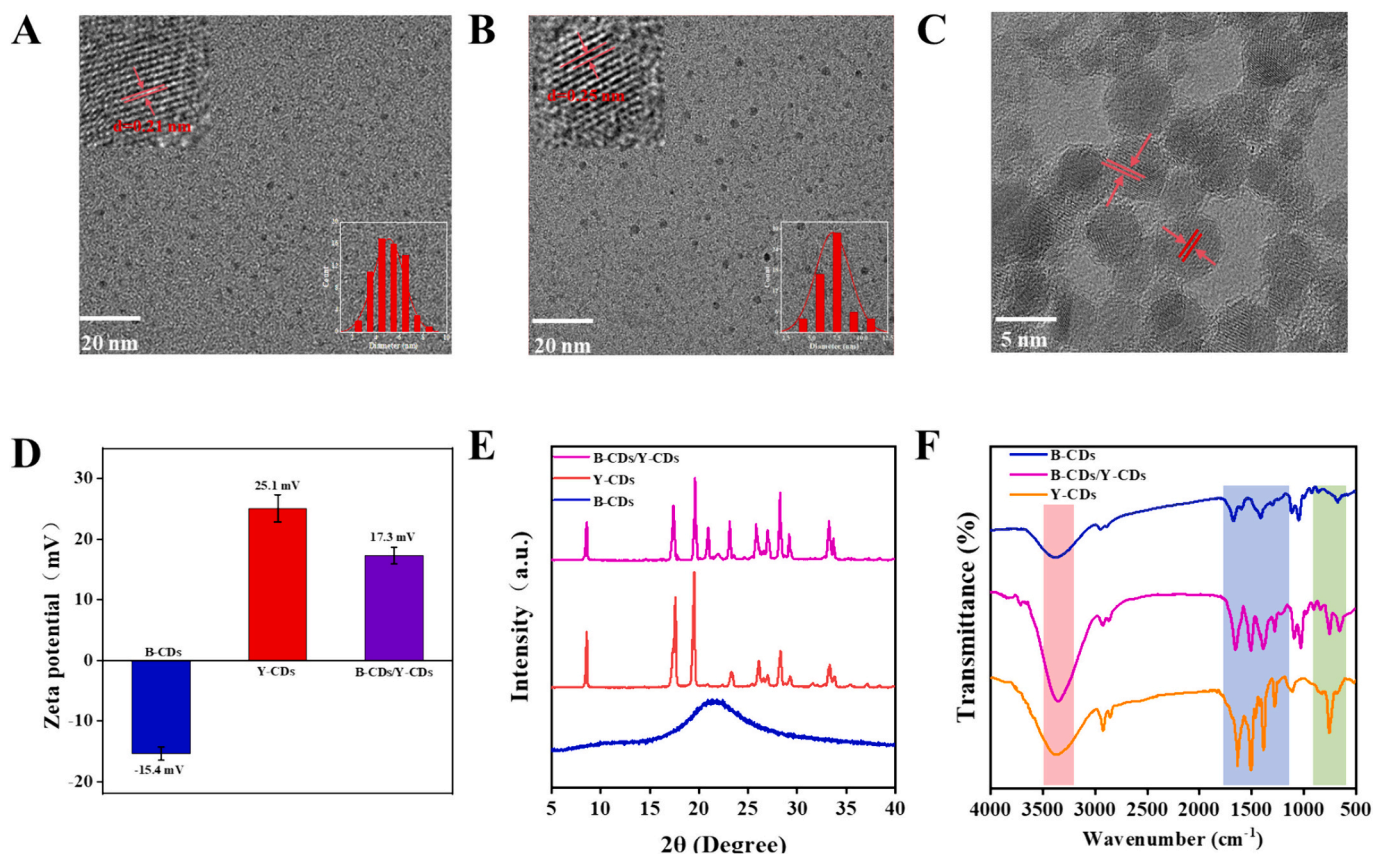


Fig. 1. TEM images of (A) B-CDs and (B) Y-CDs (inset: the histogram of the size distribution for B-CDs/Y-CDs; the HRTEM images of B-CDs and Y-CDs). (C) The HRTEM image of B-CDs/Y-CDs. (D) Zeta potential of B-CDs, Y-CDs, B-CDs/Y-CDs. (E) XRD patterns image of B-CDs (blue line), Y-CDs (red line) and B-CDs/Y-CDs (purple line). (F) FTIR spectra image of B-CDs (blue line), Y-CDs (yellow line) and B-CDs/Y-CDs (purple line). (For interpretation of the references to color in this figure legend, the reader is referred to the web version of this article.)

B-CDs + Cu^{2+} , B-CDs/Y-CDs and B-CDs/Y-CDs + Cu^{2+} were measured by FLS1000 fluorescence spectrophotometer (Edinburgh, Ltd., UK).

2.3. Construction of B-CDs/Y-CDs ratiometric fluorescent sensor

B-CDs was synthesized using the hydrothermal method in a single step (Meng et al., 2022). Simply, 0.5 g FA, 0.1 g borax and 1 mL glycerin were dispersed in 20 mL of ultra-pure water. The solution was then added into an autoclave and heated for 10 h at 160 °C. After cooling to room temperature, the solution was centrifuged at 12000 rpm for 10 min and filtered by a 0.22 μm filter. Finally, B-CDs powder was collected after freeze-drying and stored at 4 °C for future use.

Y-CDs was prepared by hydrothermal method (Lv et al., 2019). 0.6 g of OPD was dispersed in 30 mL of ultra-pure water, mixed evenly by ultrasound, and then the solution was then added into an autoclave and heated at 180 °C for 12 h. After cooling to room temperature, the solution was centrifuged at 12000 rpm for 10 min and filtered by a 0.22 μm filter. Finally, the Y-CDs powder was further dried under vacuum freezing and stored at 4 °C for use.

The ratiometric fluorescence sensor (B-CDs/Y-CDs) was obtained by simply mixing B-CDs (0.1 mg/mL, 60 μL) with Y-CDs (0.4 mg/mL, 60 μL) through electrostatic interaction.

2.4. Detection of Cu^{2+} by the B-CDs/Y-CDs sensor

A certain concentration of Cu^{2+} (0–1.4 μM , 60 μL) solution was added to the B-CDs/Y-CDs sensor, followed by PBS buffer (0.2 M, 420 μL) at pH 6, and incubated for 5 min. Then, the fluorescence spectrum of the sensor was measured, and the calibration curve was plotted

according to the relationship between Cu^{2+} concentration and the ratio of fluorescence intensity between Y-CDs and B-CDs (I_{560}/I_{460}).

2.5. Construction of the intelligent device

The intelligent device was created by integrating a smartphone (Red Mi K30s) into a portable optical detector. In generally, Cu^{2+} with different concentrations were dropped on test strips containing B-CDs/Y-CDs sensor. Then, the test strips were placed in the sample test slot of the device. Then, the fluorescence images were captured by a real-time color extraction APP in the smartphone and converted into red (R), green (G) and blue (B) values. Finally, the calibration curve between the ratio of R/B and Cu^{2+} concentration was established.

2.6. Detection of Cu^{2+} in real samples

In order to verify the practicality of the sensor, Cu^{2+} detection in actual samples was studied. Tap water and lake water as the samples were obtained from Henan Agricultural University. The food samples including fish, shrimp, crab, banana, grape, onion, parsley, carrot, cucumber, orange juice and red wine were purchased from local supermarkets.

The water and drink samples was centrifuged at 15000 rpm for 15 min, and then filtered by a microporous membrane (0.22 μm). The food samples were firstly homogenized by a homogenizer. Then, 1.0 g of samples was added into 10 mL of nitric acid and sonicated for 30 min. The mixture was heated to 150 °C for 5 h in a drying oven. After cooling, the supernatant was collected by centrifuging at 10000 rpm for 10 min. All the treated samples were diluted 10-fold with ultra-pure water.

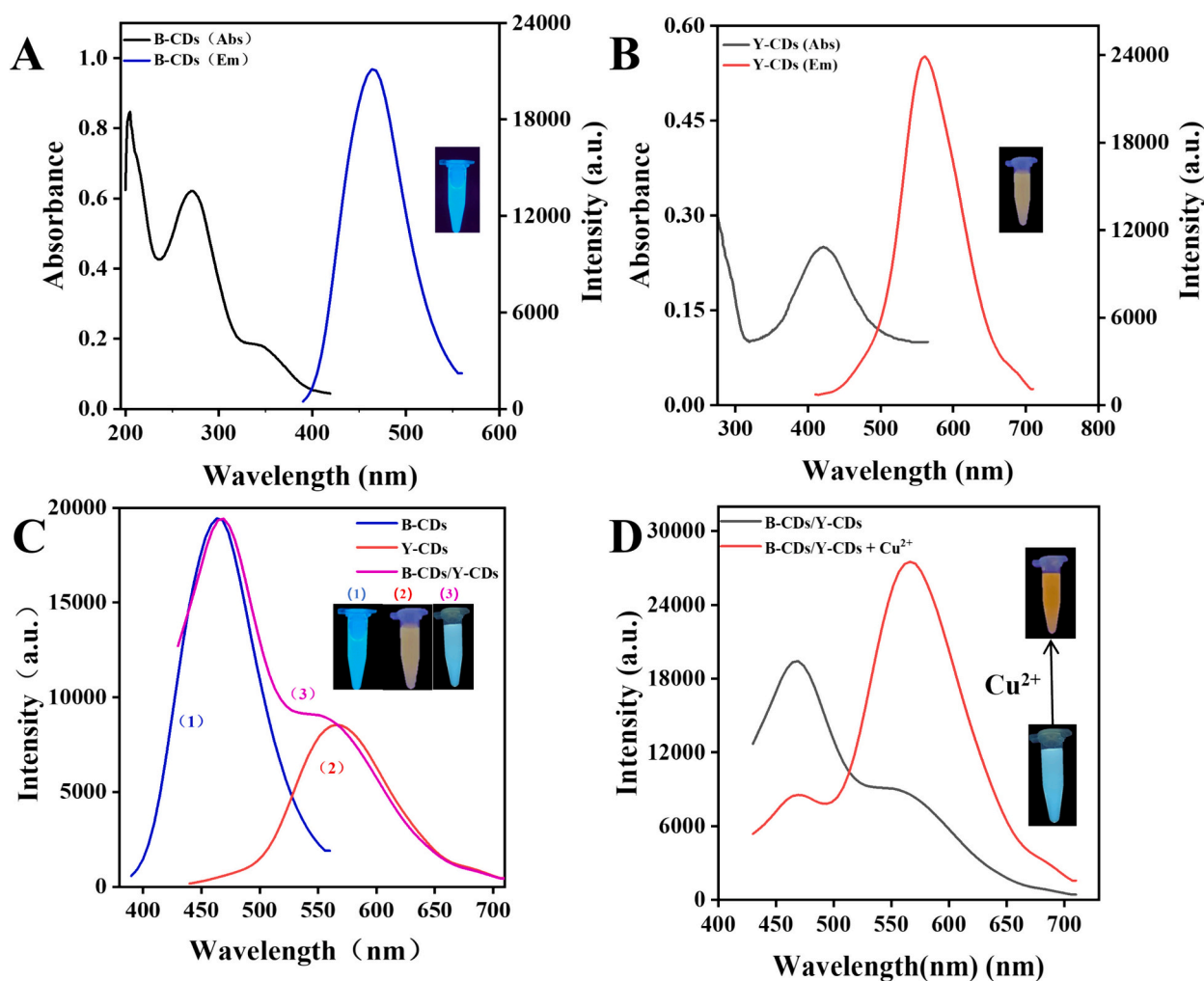


Fig. 2. UV-vis absorption spectrum and fluorescence emission spectrum of B-CDs (A) and Y-CDs (B). (C) Fluorescence spectra of B-CDs, Y-CDs and B-CDs/Y-CDs. (D) Fluorescence spectra of B-CDs/Y-CDs and B-CDs/Y-CDs + Cu^{2+} . The inset shows photos under UV lamp.

Finally, the different concentrations of Cu^{2+} (0, 0.2, 0.5 and 1.0 μM) were dispersed in the treated samples for recovery experiments. The detection process was the same as described in Section 2.4.

3. Results and discussion

3.1. Characterization of B-CDs and Y-CDs

TEM images revealed that B-CDs and Y-CDs were uniformly distributed and spherical in shape, boasting average particle sizes of 5.40 nm and 7.45 nm (Fig. 1A and B). Besides, the HRTEM image in the illustration showed that the lattice spacing is 0.21 nm and 0.25 nm, respectively. While the B-CDs/Y-CDs exhibited multi sheet morphology with mutual adsorption (Fig. C). The zeta potential of B-CDs/Y-CDs was 17.3 mV, indicating that the two CDs were combined through electrostatic adsorption (Fig. 1D) (Lin et al., 2022). The XRD of the CDs were displayed in Fig. 1E. A broad peak at about 22° suggested that the B-CDs were amorphous and highly disordered, corresponding to the (002) face of the graphite lattice (Hao et al., 2023; Wu et al., 2021; Wu et al., 2023). Y-CDs had a better crystal structure with the peaks at 8.58° , 17.6° , 19.5° , 23.3° , 26.1° , 28.3° , and 33.3° belong to the (001), (110), (-112), (020), (-212), (-112) and (-222) facets, which are in general agreement with the characteristic peaks of OPD (JCPDS 31-1831). The XRD images of B-CDs/Y-CDs showed both characteristic peaks of the two CDs, indicating that they were linked. The functional groups and chemical bonds of the CDs were investigated by FTIR. A wide absorption peak was located at

3479 cm^{-1} due to O—H stretching vibrations, confirming the existence of hydroxyl groups on the B-CDs surface (Fawaz et al., 2023; Zhang et al., 2018). The absorption peak at 1406 cm^{-1} corresponded to the stretching vibration of the C—N (Fawaz et al., 2023; Kiadeh et al., 2022). The absorption peaks at 1299 and 1045 cm^{-1} were attributed to C-B-C tensile vibration and B-O-H deformation vibration (Meng et al., 2022). The absorption peak of 1110 cm^{-1} belonged to C—N tensile vibration (Fig. 1F, blue line) (Zhao et al., 2017). The wide absorption band of Y-CDs at 3375 cm^{-1} was attributed to the stretching vibration of O—H and N—H, the two peaks at 1633 and 1506 cm^{-1} denoted the existence of unsaturated C=C and aromatic rings. The other two peaks at 1274 and 750 cm^{-1} came from C=C tensile vibration and N—H swing (Fig. 1F, red line) (An et al., 2021; Pizzoferrato et al., 2023). Besides, in Fig. 1F (purple line), the FTIR of B-CDs/Y-CDs displayed the characteristic peaks of the two CDs, indicating the successful connection of the two CDs. The elemental composition and chemical bonding of the CDs were analyzed by XPS. The raw XPS data indicated that the B-CDs was mainly composed of carbon (C), nitrogen (N) and oxygen (O) (Fig. S1A in Supporting Information (SI)). The spectrum of C1s showed five bond energy peaks at 285.6, 286.3, 285.6, 284.9, and 283.9 eV, corresponding to the C=O, C—O, C=C, C—N, and C—B groups, respectively (Fig. S1B). The spectrum of N1s exhibited two peaks at 398.9 and 395.8 eV, which were attributed to N—H and N—C, respectively (Fig. S1C). The O1s spectrum showed three peaks at 532.6, 531.6 and 531.4 eV, corresponding to N—O, C—O and C—OH respectively (Fig. S1D). Fig. S1E illustrated the element composition of Y-CDs. The C1s spectrum showed

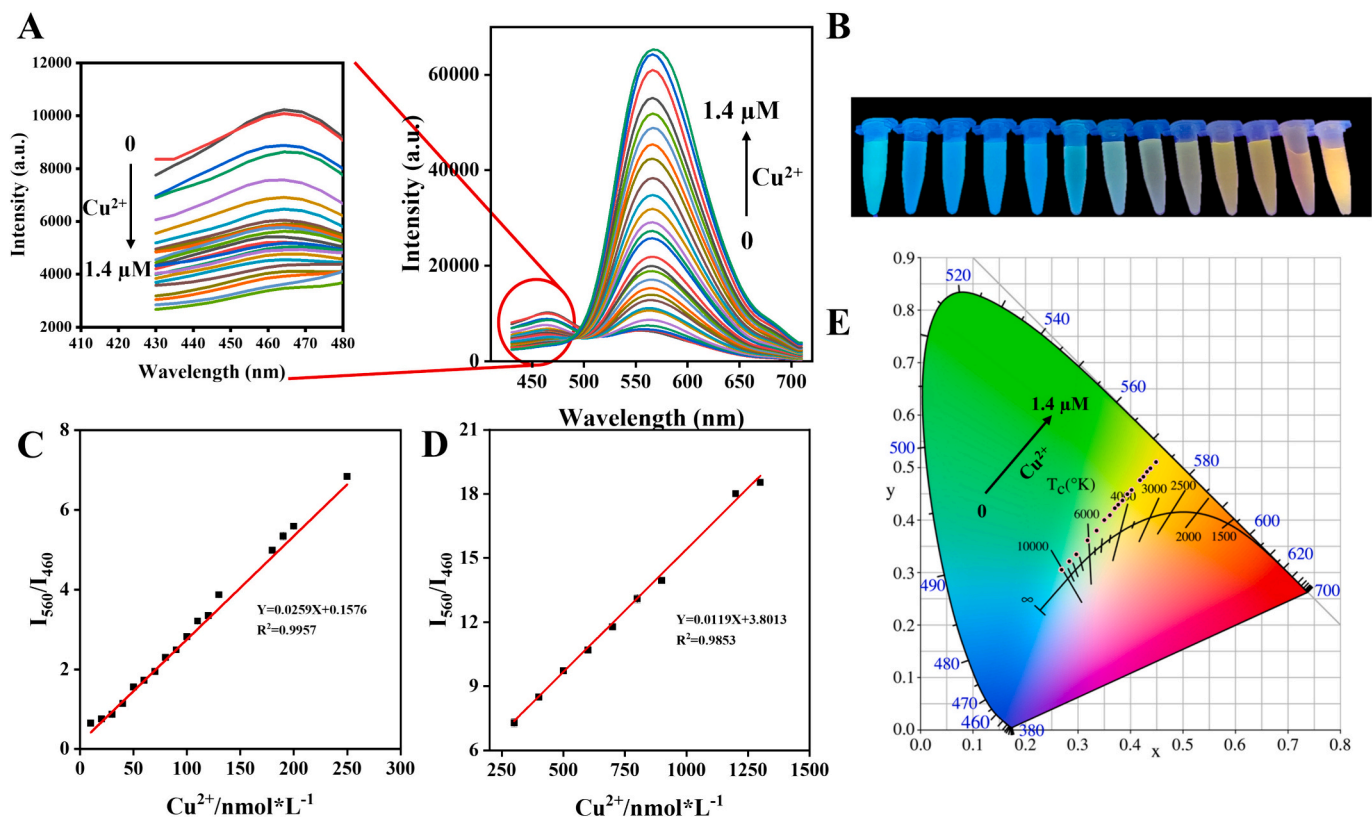


Fig. 3. (A) The fluorescence spectrum of the B-CDs/Y-CDs in the Cu^{2+} concentration range of 0–1.4 $\mu\text{mol/L}$. (B) The corresponding color change under a UV lamp. The I_{560}/I_{460} was linear with Cu^{2+} concentration in range of (C) 10–250 nmol/L and (D) 300–1300 nmol/L. (E) CIE chromaticity diagram from the fluorescence spectra of B-CDs/Y-CDs with different concentrations of Cu^{2+} .

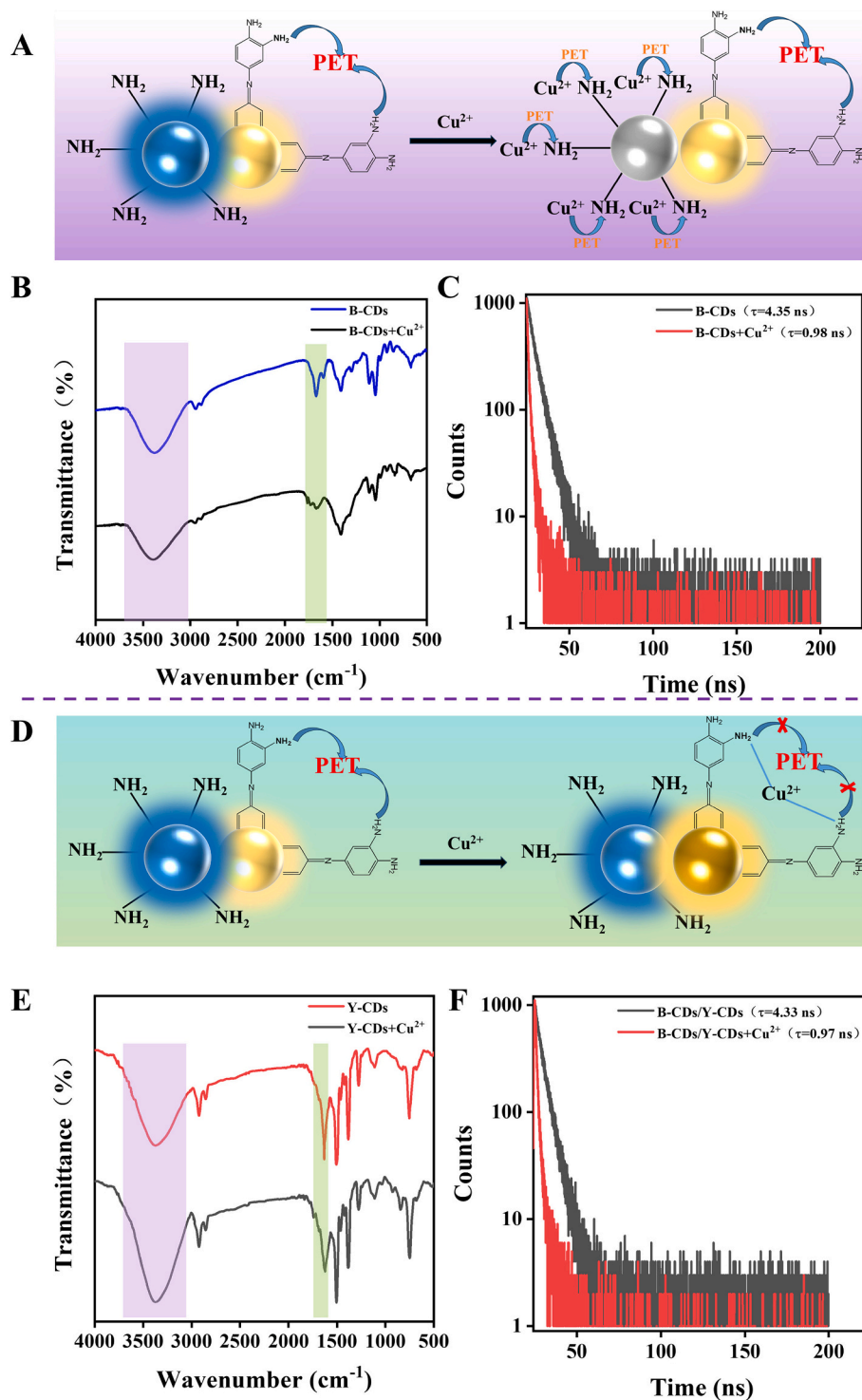


Fig. 4. (A) The sensing mechanism of B-CDs and Cu^{2+} . (B) FTIR spectrum of B-CDs and B-CDs + Cu^{2+} . (C) Fluorescence lifetime of B-CDs and B-CDs + Cu^{2+} . (D) The sensing mechanism of Y-CDs and Cu^{2+} . (E) FTIR spectrum of Y-CDs and Y-CDs + Cu^{2+} . (F) Fluorescence lifetime of B-CDs/Y-CDs and B-CDs/Y-CDs + Cu^{2+} .

three peaks at 284.8, 284.9, and 285.6 eV, corresponding to C=C, C-N, and C-O, respectively (Fig. S1F). The N1s spectrum presented three peaks at 399.3, 398.5, and 398.1 eV, belonging to N-H, N-C-N, and N-(C)₃, respectively (Fig. S1G). The O1s spectrum exhibited two peaks at 531.9 and 531.5 eV, corresponding to C=O and C-OH/C-O-C, respectively (Fig. S1H).

3.2. The fluorescence characteristics and stability of B-CDs/Y-CDs

As displayed in Fig. 2A, B-CDs had a bright blue fluorescence under UV irradiation. In addition, the absorption spectra of B-CDs contained two characteristic peaks at 276 nm and 347 nm, which were related to the electron leaps from π (or n) to π^* in the aromatic sp^2 structural domain (C=C) and aromatic heterocycles (C=N and C=O), respectively (Meng et al., 2022; Yu et al., 2022; Zhao et al., 2017). Y-CDs exhibited a dim yellow fluorescence (Fig. 2B). The wide absorption peak of Y-CDs at

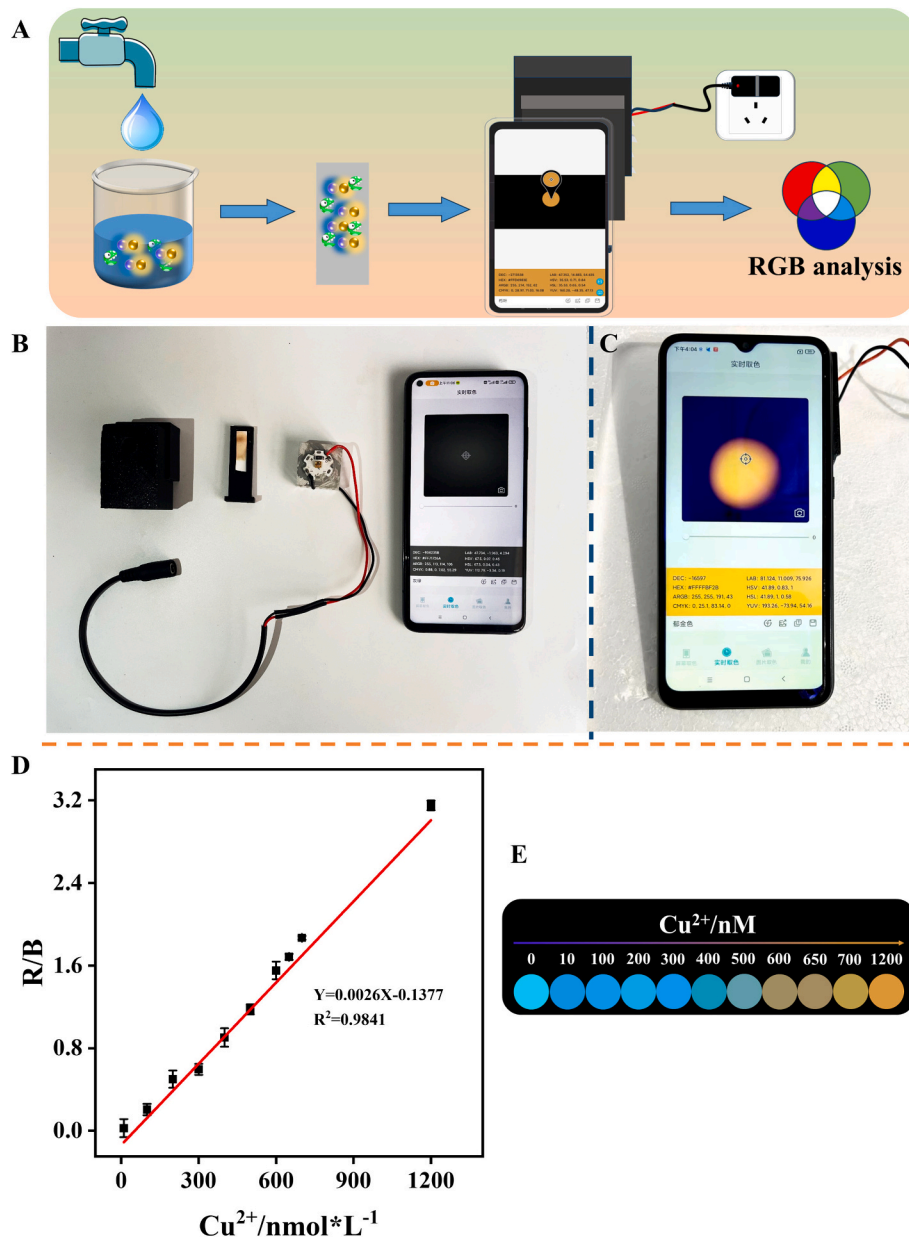


Fig. 5. (A) Schematic diagram of intelligent device detecting Cu²⁺. (B) Composition of intelligent device. (C) The intelligent device was used to visual on-site and POCT of Cu²⁺. (D) The value of R/B was linear with Cu²⁺ at 10–1200 nmol/L; (E) Fluorescence color changed corresponding to Cu²⁺ concentration.

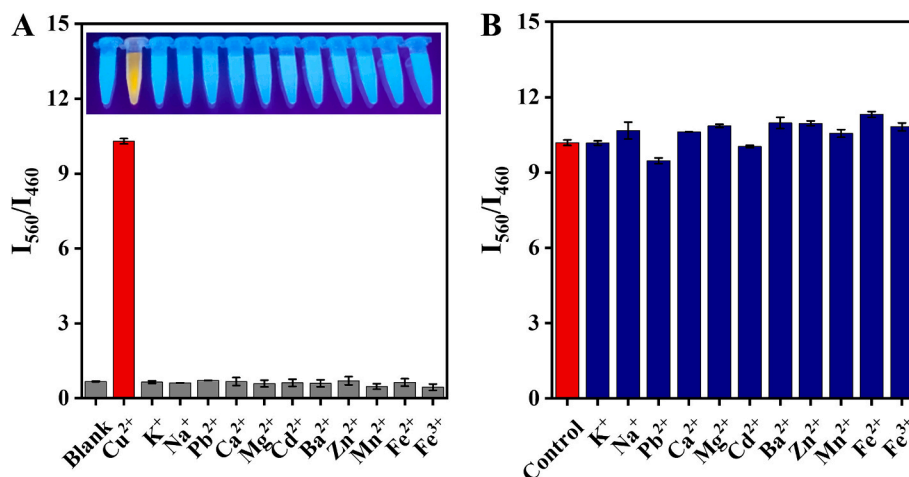


Fig. 6. (A) Selectivity and (B) anti-interference of Cu²⁺ detected by B-CDs/Y-CDs sensor.

around 410 nm originates from the n-p* jump (Lv et al., 2019). Upon excitation at 400 nm, B-CDs/Y-CDs maintained their emission peaks at 460 nm for B-CDs and 560 nm for Y-CDs (Fig. S2 and 2C). Upon exposure to Cu²⁺, the fluorescence intensity of B-CDs diminished, whereas that of Y-CDs heightened via PET. As a result, the fluorescence color shifted from blue to yellow (Fig. 2D). Therefore, a ratiometric fluorescent sensor B-CDs/Y-CDs for Cu²⁺ detection was constructed.

3.3. Optimization of sensing conditions

To enhance the sensing capability of Cu²⁺, the pH level of the buffer solution and the incubation duration of the B-CDs/Y-CDs sensor were meticulously optimized. The fluorescence ratio changes at different pH (3–8) were measured. In the absence of Cu²⁺, the fluorescence ratio I_{560}/I_{460} did not increase with the increase of pH, indicating that B-CDs/Y-CDs remained stable at different pH (Fig. S3 A). When exposed to Cu²⁺, the value of I_{560}/I_{460} gradually increases as the pH level rises, reaching its peak at pH = 6 before gradually declining as the pH level continues to increase. Therefore, the subsequent experiment was conducted with pH = 6. Fig. S3B shows that after the addition of Cu²⁺, there was a significant increase in I_{560}/I_{460} , which stabilized after 5 min. Consequently, a 5-min incubation period was adopted for subsequent experiments.

3.4. Ratiometric detection of Cu²⁺ by the B-CDs/Y-CDs sensor

Fig. 3A illustrated the changes of fluorescence spectra of B-CDs/Y-CDs as Cu²⁺ concentration increases from 0 to 1.4 μM. As the concentration of Cu²⁺ increased, the fluorescence intensity of Y-CDs rose, whereas the fluorescence intensity of B-CDs declined. The fluorescent colors changed significantly from blue to yellow (Fig. 3 B) which was confirmed by CIE coordinates (from blue area to yellow area) (Fig. 3E). In the range of 10–250 nM and 300–1300 nM, there were linear relationships between the fluorescence ratio I_{560}/I_{460} and the concentration of Cu²⁺, and the equations were $Y = 0.0259x + 0.1576$, $R^2 = 0.9957$; $Y = 0.0115x + 3.9342$, $R^2 = 0.9973$, respectively (Fig. 3C and D). According to Limit of detection (LOD) = 3σ/K, the LOD was 2.29 nM. Compared with some previously reported fluorescence sensors, the sensor had excellent sensitivity for Cu²⁺ detection (Table. S1).

3.5. Possible fluorescence mechanism

It was found that the fluorescence of B-CDs was obviously quenched once exposed to Cu²⁺. We theorized that the cause of the quenching of B-CDs was the formation of a B-CDs/Cu²⁺ complex, which occurred through coordination interactions with the amino groups on the surface of B-CDs, leading to fluorescence quenching of B-CDs via PET processes

(Fig. 4A) (Gao et al., 2015). Fig. S4A shown that the absorption spectrum of B-CDs shifted after the introduction of Cu²⁺. Additionally, the zeta potential of B-CDs rose from −15.4 mV to 3.3 mV (Fig. S4B) (Azami et al., 2024). The FTIR spectra of B-CDs/Cu²⁺ showed significant changes at 1444 and 3100–3500 cm^{−1}, indicating that Cu²⁺ interacted with the amino groups of B-CDs (Fig. 4B) (Yakusheva et al., 2023). Further, the fluorescence lifetime of B-CDs before and after adding Cu²⁺ was measured at an emission wavelength of 460 nm. In Fig. 4C, compared with free B-CDs, the lifetime of B-CDs + Cu²⁺ decreased from 4.35 ns to 0.98 ns, proving that the process was dynamic quenching. For the Y-CDs, we speculated that the increasing of Y-CDs was due to the formation of Y-CDs/Cu²⁺ complex by Cu²⁺ through coordination interactions with amino groups on the surface of Y-CDs, inhibiting the PET process of the internal self of Y-CDs (Fig. 4D). Fig. S5 A shown that the absorption peak of Y-CDs was gradually increased which triggered by Cu²⁺, indicating that formation of Y-CDs/Cu²⁺ complex (Pizzoferrato et al., 2023). The zeta potential of Y-CDs also dropped from 25.1 mV to 11.5 mV (Fig. S5B) (Wang et al., 2017). The FTIR spectra of Y-CDs changed significantly at 1633 and 3375 cm^{−1}, showing that the chelation of amino group and Cu²⁺ (Fig. 4E) (Yakusheva et al., 2023). The lifetime of B-CDs/Y-CDs + Cu²⁺ was dropped to 0.97 ns (Fig. 4F). All these results could provide strong evidence for the hypothesis we mentioned.










3.6. Intelligent device assisted with smartphone for visible POCT of Cu²⁺

In order to meet the needs of social development, an intelligent device was constructed for visual and POCT of Cu²⁺ on-site (Fig. 5A). The device is composed of a smartphone, a camera obscura, an ultraviolet lamp and a sample test paper slot (Fig. 5B). After adding Cu²⁺ on the test strip, the fluorescence color was captured and converted to RGB values by smartphone (Fig. 5C). Fig. 5D shown that the values of R/B increased linearly as the Cu²⁺ concentration (10–1200 nM) increased. The regression equations were expressed as $R/B = 0.0026x - 0.1377$, with R^2 of 0.9841 and LOD of 7.51 nM. More importantly, the fluorescence color also can be observed from blue to yellow (Fig. 5E).

3.7. Selectivity and interference investigation















To evaluate the selectivity and anti-interference of B-CDs/Y-CDs sensor, different metal ions were added to the sensor. Fig. 6A shown that the value of I_{560}/I_{460} increases significantly with the fluorescence color changed into yellow. In addition, after adding equal amounts of different metal ions to the sensor containing Cu²⁺. It was found that the value of I_{560}/I_{460} changed slightly, compared to the control results (Fig. 5B). Overall, the sensor can detect Cu²⁺ in complex samples without

Table 1
Detection of Cu²⁺ in spiked samples by the intelligent device, sensor and ICP-MS (n = 3).

Samples	Spiked (μM)	Intelligent device			This work			ICP-MS			
		Visualization	Test value (μM)	Recovery (%)	RSD (%)	Test value (μM)	Recovery (%)	RSD (%)	Test value (μM)	Recovery (%)	RSD (%)
All Samples	0		0	–	–	0	–	–	0	–	–
	0.2		0.204	102.0	3.42	0.209	104.5	1.54	0.201	100.5	0.09
Tap water	0.5		0.522	104.4	3.74	0.488	97.6	1.89	0.509	101.8	0.27
	1.0		1.079	107.9	5.22	1.054	105.4	3.45	0.986	98.6	0.97
Lake water	0.2		0.185	92.5	3.12	0.191	95.5	2.42	0.196	98.0	0.12
	0.5		0.467	93.4	4.26	0.486	97.2	3.78	0.511	102.2	0.26
	1.0		1.104	110.4	5.33	1.087	108.7	4.93	1.036	103.6	0.89
Fish	0.2		0.192	96.0	2.91	0.211	105.5	1.96	0.207	103.5	0.11
	0.5		0.543	108.6	4.25	0.535	107.0	3.74	0.511	102.2	0.36
	1.0		0.922	92.2	5.57	0.946	94.6	5.44	1.039	103.9	0.84
Shrimp	0.2		0.182	91.0	3.46	0.191	95.5	1.95	0.202	101.0	0.11
	0.5		0.539	107.8	4.21	0.489	97.8	2.98	0.492	98.4	0.31
	1.0		1.098	109.8	5.49	1.075	107.5	5.12	0.988	98.8	0.67
Crab	0.2		0.187	93.5	3.07	0.191	95.5	2.93	0.205	102.5	0.12
	0.5		0.474	94.8	3.45	0.522	104.4	3.09	0.519	103.8	0.22
	1.0		1.115	111.5	5.88	1.098	109.8	4.96	0.991	99.1	0.45
Banana	0.2		0.219	109.5	2.24	0.211	105.5	1.98	0.204	102.0	0.09
	0.5		0.546	109.2	3.78	0.534	106.8	3.34	0.517	103.4	0.48
	1.0		0.934	93.4	4.98	0.937	93.7	4.66	1.041	104.1	0.94
Grape	0.2		0.225	112.5	3.39	0.219	109.5	3.19	0.207	103.5	0.11
	0.5		0.549	109.8	4.45	0.541	108.2	4.12	0.496	99.2	0.33
	1.0		1.127	112.7	6.07	1.109	110.9	5.23	1.033	103.3	0.97
Onion	0.2		0.188	94.0	2.34	0.212	106.0	2.29	0.204	102.0	0.08
	0.5		0.539	107.8	3.96	0.531	106.2	3.34	0.494	98.8	0.35
	1.0		1.104	110.4	5.52	1.089	108.9	5.57	1.017	101.7	0.64
Orange juice	0.2		0.214	107.0	1.97	0.211	105.5	1.67	0.203	101.5	0.09

(continued on next page)

Table 1 (continued)

Samples	Spiked (μM)	Visualization	Intelligent device			This work			ICP-MS		
			Test value (μM)	Recovery (%)	RSD (%)	Test value (μM)	Recovery (%)	RSD (%)	Test value (μM)	Recovery (%)	RSD (%)
Red wine	0.5		0.468	93.6	2.26	0.487	97.4	2.08	0.509	101.8	0.26
	1.0		1.066	106.6	5.19	1.037	103.7	4.78	0.993	99.3	0.64
	0.2		0.179	89.5	3.56	0.186	93.0	2.87	0.198	99.0	0.08
	0.5		0.457	91.4	4.43	0.469	93.8	4.07	0.496	99.2	0.17
	1.0		0.947	94.7	5.88	0.943	94.3	5.12	0.989	98.9	0.65
Parsley	0.2		0.184	92.0	2.47	0.186	93.0	2.49	0.198	99.0	0.09
	0.5		0.557	111.4	4.55	0.479	95.8	2.98	0.512	102.4	0.19
	1.0		0.941	94.1	5.51	1.047	104.7	4.34	1.027	102.7	0.49
Carrot	0.2		0.211	105.5	2.34	0.194	97.0	1.56	0.198	99.0	0.27
	0.5		0.533	106.6	4.98	0.515	103.0	3.31	0.497	99.4	0.14
	1.0		1.089	108.9	5.64	1.045	104.5	4.11	1.012	101.2	0.36
Cucumber	0.2		0.180	90.0	3.17	0.194	97.0	2.22	0.195	97.5	0.09
	0.5		0.446	89.2	3.68	0.472	94.4	3.23	0.491	98.2	0.16
	1.0		0.921	92.1	5.73	1.041	104.1	4.85	1.011	101.1	0.32

interference from other ions.

3.8. Real sample analysis

To assess the viability of the fabricated B-CDs/Y-CDs sensor and the intelligent device in real-life samples. The concentration of Cu^{2+} in water and food samples was measured by spiked recovery method. Cu^{2+} standard solution of 0, 0.2, 0.5 and 1.0 μM were added to the samples, respectively. The results were presented in Table 1, where the recoveries ranged from 93.7 % to 110.9 % for the sensor with the relative standard deviations (RSD) not exceeding 5.57 %. And the recoveries ranged from 89.2 % to 112.7 % for the intelligent device with RSD not exceeding 6.07 %. The changes in fluorescence were observed with the as the concentration of Cu^{2+} increased in various samples. Furtherly, the results were basically consistent with those of ICP-MS, demonstrating the applicability of the sensor and intelligent device for Cu^{2+} detection.

4. Conclusions

In conclusion, a ratiometric fluorescence sensor B-CDs/Y-CDs was developed for rapid and sensitive detection of Cu^{2+} . The addition of Cu^{2+} could interact with the amino group on the surface of B-CDs and Y-CDs, resulting in a PET reaction between Cu^{2+} and the two types of CDs, which quenches the fluorescence of B-CDs and enhances the fluorescence of Y-CDs. The LOD of 2.29 nM can satisfy the detection level of Cu^{2+} in the actual sample. In addition, an intelligent device combining smartphone and optical detector is assembled for on-site visualization and POCT of Cu^{2+} with a LOD of 7.51 nM. The strategy has an excellent

potential to improve the detection efficiency and reduce the losses, showing important practical significance in food safety and environmental pollution.

Funding

This work was supported by the National Natural Science Foundation of China (NO. 32101966), the Natural Science Foundation of Henan Province (NO. 232300421259), the Young Talents Project of Henan Agricultural University (NO. 30501303), National Key Research and Development Program of China (NO. 2022YFD2100505), the Program for Innovative Research Team (in Science and Technology) in university of Henan Province (NO. 23IRTSTHN023).

CRediT authorship contribution statement

Tiang Li: Writing – original draft, Methodology, Formal analysis, Data curation. **Meiju Lu:** Validation, Investigation. **Ning Li:** Visualization, Supervision. **Yan Ma:** Validation, Supervision. **Lianjun Song:** Supervision, Conceptualization. **Xianqing Huang:** Visualization, Validation, Conceptualization. **Jiansheng Zhao:** Validation, Conceptualization. **Tianlin Wang:** Investigation, Formal analysis, Data curation.

Declaration of competing interest

The authors declare that they have no known competing financial interests or personal relationships that could have appeared to influence the work reported in this paper.

Data availability

Data will be made available on request.

Appendix A. Supplementary data

Supplementary data to this article can be found online at <https://doi.org/10.1016/j.fochx.2024.101834>.

References

- Al Mashhadany, Y., Alsanad, H. R., Al-Askari, M. A., Algburi, S., & Taha, B. A. (2024). Irrigation intelligence—Enabling a cloud-based internet of things approach for enhanced water management in agriculture. *Environmental Monitoring and Assessment*, 196(5), 438. <https://doi.org/10.1007/s10661-024-12606-1>
- Alafeef, M., Srivastava, I., Aditya, T., & Pan, D. (2024). Carbon dots: From synthesis to unraveling the fluorescence mechanism. *Small*, 20(4), Article 2303937. <https://doi.org/10.1002/sml.202303937>
- An, Y., Lin, X., Zhou, Y., Li, Y., Zheng, Y., Wu, C., ... Liu, C. (2021). Red, green, and blue light-emitting carbon dots prepared from o-phenylenediamine. *RSC Advances*, 11(43), 26915–26919. <https://doi.org/10.1039/D1RA02298A>
- Azami, M., Valizadehderakhshan, M., Tukur, P., & Wei, J. (2024). Highly fluorescent N, B-doped carbon nanodots performing as optical turn-off probes discerning Fe (II). *Journal of Photochemistry and Photobiology A: Chemistry*, 446, Article 115111. <https://doi.org/10.1016/j.jphotochem.2023.115111>
- Chen, Q., Wang, Y., Zhai, J., & Xie, X. (2023). Photoswitchable hemithioindigo inspired copper ion selective sensing with excellent selectivity and versatile operational modes. *Sensors and Actuators B: Chemical*, 381, Article 133437. <https://doi.org/10.1016/j.snb.2023.133437>
- Fawaz, W., Hasian, J., & Alghoraibi, I. (2023). Synthesis and physicochemical characterization of carbon quantum dots produced from folic acid. *Scientific Reports*, 13(1), Article 18641. <https://doi.org/10.1038/s41598-023-46084-1>
- Gao, Z., Wang, L., Su, R., Huang, R., Qi, W., & He, Z. (2015). A carbon dot-based “off-on” fluorescent probe for highly selective and sensitive detection of phytic acid. *Biosensors and Bioelectronics*, 70, 232–238. <https://doi.org/10.1016/j.bios.2015.03.043>
- Ge, J., Shen, Y., Wang, W., Li, Y., & Yang, Y. (2021). N-doped carbon dots for highly sensitive and selective sensing of copper ion and sulfide anion in lake water. *Journal of Environmental Chemical Engineering*, 9(2), Article 105081. <https://doi.org/10.1016/j.jece.2021.105081>
- Hao, Y., Li, R., Liu, Y., Zhang, X., Geng, L., & Chen, S. (2023). The on-off-on fluorescence sensor of hollow carbon dots for detecting Hg²⁺ and ascorbic acid. *Journal of Fluorescence*, 33(2), 459–469. <https://doi.org/10.1007/s10895-022-03057-3>
- Kiadeh, S. Z. H., Ghaee, A., Pishbin, F., Nourmohammadi, J., & Farokhi, M. (2022). Nanocomposite pectin fibers incorporating folic acid-decorated carbon quantum dots. *International Journal of Biological Macromolecules*, 216, 605–617. <https://doi.org/10.1016/j.ijbiomac.2022.07.031>
- Liang, M., Gao, Y., Sun, X., Kong, R. M., Xia, L., & Qu, F. (2024). Metal-organic framework-based ratiometric point-of-care testing for quantitative visual detection of nitrite. *Journal of Hazardous Materials*, 469, Article 134021. <https://doi.org/10.1016/j.jhazmat.2024.134021>
- Lin, Q., Chu, H., Chen, J., Gao, L., Zong, W., Han, S., & Li, J. (2022). Dual-emission ratiometric fluorescence probe based on copper nanoclusters for the detection of rutin and picric acid. *Spectrochimica Acta Part A: Molecular and Biomolecular Spectroscopy*, 270, Article 120829. <https://doi.org/10.1016/j.saa.2021.120829>
- Liu, K., Guo, Y., Yu, H., Cheng, Y., Xie, Y., & Yao, W. (2023). Sulfhydryl-functionalized carbon dots as effective probes for fluorescence enhancement detection of patulin. *Food Chemistry*, 420, Article 136037. <https://doi.org/10.1016/j.foodchem.2023.136037>
- Liu, P., Hao, R., Sun, W., & Li, J. (2023). Ratiometric detection of Cu²⁺ in water and drinks using Tb (iii)-functionalized UiO-66-type metal-organic frameworks. *Analytical Methods*, 15(16), 1953–1958. <https://doi.org/10.1039/D3AY00044C>
- Lledó, D., Grindlay, G., Serrano, R., Gras, L., & Sansano, J. M. (2023). Imidazolium-based task-specific ionic liquid for selective Ag, Cu, Pd and Pt determination by means of dispersive liquid-liquid microextraction and inductively coupled plasma optical emission spectrometry. *Spectrochimica Acta Part B: Atomic Spectroscopy*, 204, Article 106672. <https://doi.org/10.1016/j.sab.2023.106672>
- Lu, M., Zhang, Y., Li, S., Zhang, Y., Fang, S., Yang, W., ... Wang, H. (2023). A novel colorimetric/fluorescent dual-signal probe based on silver nanoparticles functionalized with L-cysteine and rhodamine 6G derivatives for copper ion detection and cell imaging. *Environmental Research*, 236, Article 116540. <https://doi.org/10.1016/j.envres.2023.116540>
- Lu, Y., Wei, X., Chen, M., & Wang, J. (2023). Non-ceruloplasmin-bound copper and copper speciation in serum with extraction using functionalized dendritic silica spheres followed by ICP-MS detection. *Analytica Chimica Acta*, 1251, Article 340993. <https://doi.org/10.1016/j.aca.2023.340993>
- Lv, W., Lin, M., Li, R., Zhang, Q., Liu, H., Wang, J., & Huang, C. (2019). Aggregation-induced emission enhancement of yellow photoluminescent carbon dots for highly selective detection of environmental and intracellular Copper (II) ions. *Chinese Chemical Letters*, 30(7), 1410–1414. <https://doi.org/10.1016/j.ccl.2019.04.011>
- Meng, A., Huangfu, B., Sheng, L., Hong, X., & Li, Z. (2022). One-pot hydrothermal synthesis of boron and nitrogen co-doped carbon dots for copper ion assay and multicolor cell imaging using fluorescence quenchometric method. *Microchemical Journal*, 174, Article 106981. <https://doi.org/10.1016/j.microc.2021.106981>
- Miao, J., Yu, J., Zhao, X., Chen, X., Zhu, C., Cao, X., ... Wang, X. (2024). Molecular imprinting-based triple-emission ratiometric fluorescence sensor with aggregation-induced emission effect for visual detection of doxycycline. *Journal of Hazardous Materials*, 470, Article 134218. <https://doi.org/10.1016/j.jhazmat.2024.134218>
- Moussouli, S., Smaili, F., Berrabah, S. E., & Manseri, A. (2023). Fabrication of novel electrochemical sensor based on NiO-nanoparticles for copper detection in drinking water. *Inorganic Chemistry Communications*, 158, Article 111563. <https://doi.org/10.1016/j.inoche.2023.111563>
- Pizzoferrato, R., Bisariya, R., Antonaroli, S., Cabibbo, M., & Moro, A. J. (2023). Colorimetric and fluorescent sensing of copper ions in water through o-phenylenediamine-derived carbon dots. *Sensors*, 23(6), 3029. <https://doi.org/10.3390/s23063029>
- Pourbasheer, E., Morsali, S., Ansari, S., Mirtamizdoust, B., Vojoudi, H., & Ganjali, M. R. (2022). Extraction of trace quantities of copper using novel modified magnetite nanoparticles for atomic absorption spectrometry analysis. *Current Analytical Chemistry*, 18(8), 907–913. <https://www.eurekaselect.com/article/124205>
- Speranskaya, E. S., Drozd, D. D., Pidenko, P. S., & Goryacheva, I. Y. (2020). Enzyme modulation of quantum dot luminescence: Application in bioanalysis. *TrAC Trends in Analytical Chemistry*, 127, Article 115897. <https://doi.org/10.1016/j.trac.2020.115897>
- Wang, J., Li, R. S., Zhang, H. Z., Wang, N., Zhang, Z., & Huang, C. Z. (2017). Highly fluorescent carbon dots as selective and visual probes for sensing copper ions in living cells via an electron transfer process. *Biosensors and Bioelectronics*, 97, 157–163. <https://doi.org/10.1016/j.bios.2017.05.035>
- Wang, Y., Ma, Y., Wang, H., Shang, F., Yang, B., & Han, Y. (2024). Smartphone-assisted carbon dots fluorescent sensing platform for visual detection of Thiophanate-methyl in fruits and vegetables. *Food Chemistry*, 441, Article 138413. <https://doi.org/10.1016/j.foodchem.2024.138413>
- Wu, Y., Zuo, C., Mou, Y., Wang, H., Hou, Y., Su, X., ... Qiu, H. (2023). One step synthesis of highly photoluminescent red light-emitting carbon dots from O-phenylenediamine and 2, 4-diaminophenol as fluorescent probes for the detection of pH and Cr (vi). *Analytical Methods*, 15(42), 5607–5619. <https://doi.org/10.1039/D3AY01323E>
- Wu, Z., Chen, R., Pan, S., Liu, H., & Hu, X. (2021). A ratiometric fluorescence strategy based on dual-signal response of carbon dots and o-phenylenediamine for ATP detection. *Microchemical Journal*, 164, Article 105976. <https://doi.org/10.1016/j.microc.2021.105976>
- Xu, J., Wang, Y., Huang, M., Xu, X., Zeng, Y., Luo, X., ... Zhong, W. (2023). Self-assembling NBD-tripeptide as a dual-mode colorimetric platform for naked eye and smartphone joint detection of micro to nanomolar Copper (II) ions. *Talanta*, 261, Article 124662. <https://doi.org/10.1016/j.talanta.2023.124662>
- Yakusheva, A., Aly-Eldeen, M., Gusev, A., Zakharova, O., & Kuznetsov, D. (2023). Cyan fluorescent carbon quantum dots with amino derivatives for the visual detection of Copper (II) cations in sea water. *Nanomaterials*, 13(6), 1004. <https://doi.org/10.3390/nano13061004>
- Yu, M., Guo, X., Lu, H., Li, P., Huang, R., Xu, C., ... Xing, X. (2022). Carbon dots derived from folic acid as an ultra-succinct smart antimicrobial nanosystem for selective killing of *S. aureus* and biofilm eradication. *Carbon*, 199, 395–406. <https://doi.org/10.1016/j.carbon.2022.07.065>
- Zeng, M. H., Zhang, C., Yao, Q. H., Jin, J. W., Ye, T. X., Chen, X. M., ... Chen, X. (2024). Multifunctional nanoenzyme-assisted ion-selective and oxidation catalysis SERS biosensors for point-of-care nitrite testing. *Sensors and Actuators B: Chemical*, 405, Article 135352. <https://doi.org/10.1016/j.snb.2024.135352>
- Zhang, J., Zhao, X., Xian, M., Dong, C., & Shuang, S. (2018). Folic acid-conjugated green luminescent carbon dots as a nanoprobe for identifying folate receptor-positive cancer cells. *Talanta*, 183, 39–47. <https://doi.org/10.1016/j.talanta.2018.02.009>
- Zhang, M., Yin, H., Wan, L., Gao, H., Liu, S., & Liu, Y. (2024). The fluorescent and colorimetric dual-response sensor based on carbon dots doped with nitrogen and sulfur for detecting copper ions. *Carbon Letters*, 34, 1155–1164. <https://doi.org/10.1007/s42823-023-00682-1>
- Zhang, S., Xiao, J., Zhong, G., Xu, T., & Zhang, X. (2024). Design and application of dual-emission metal-organic frameworks-based ratiometric fluorescence sensors. *Analyst*, 149, 1381–1397. <https://doi.org/10.1039/D3AN02187D>
- Zhao, N., Song, J., Huang, Z., Yang, X., Wang, Y., & Zhao, L. (2021). Ratiometric fluorescence probe of Cu²⁺ and bi thiols by using carbon dots and copper nanoclusters. *RSC Advances*, 11(53), 33662–33674. <https://doi.org/10.1039/D1RA05854A>
- Zhao, X., Zhang, J., Shi, L., Xian, M., Dong, C., & Shuang, S. (2017). Folic acid-conjugated carbon dots as green fluorescent probes based on cellular targeting imaging for recognizing cancer cells. *RSC Advances*, 7(67), 42159–42167. <https://doi.org/10.1039/C7RA07002K>
- Zuo, Y. N., Liu, S., Zhao, X. E., Zhu, S., & Xu, G. (2023). Tb-metal organic frameworks-referenced bathocuproine disulfonate enable fluorescence distinguishing Cu⁺ from Cu²⁺. *Sensors and Actuators B: Chemical*, 394, Article 134487. <https://doi.org/10.1016/j.snb.2023.134487>